Postprint of: Knozowski D., Vallachira Warriam Sasikumar P., Dubey R., Aebli M., Kravchyk K. V., Trykowski G., Kovalenko M. V., Graule T., Wilamowska-Zawłocka M., Blugan G., Silicon oxycarbide-tin nanocomposite derived from a UV crosslinked single source preceramic precursor as high-performance anode materials for Li-ion batteries, Applied Materials Today Vol. 27, (2022), 101424, DOI: 10.1016/j.apmt.2022.101424

Silicon oxycarbide-tin nanocomposite derived from a UV crosslinked single source preceramic precursor as high-performance anode materials for Li-ion batteries

*Dominik Knozowski‡ [a], Pradeep Vallachira Warriam Sasikumar‡ [b], Romain Dubey [c, d], Marcel Aebli [c, d], Kostiantyn V. Kravchyk [c, d], Grzegorz Trykowski [e], Maksym V. Kovalenko [c, d], Thomas Graule [b], Monika Wilamowska-Zawłocka [a, *], Gurdial Blugan [b, *]*

[a] Department of Energy Conversion and Storage, Faculty of Chemistry, Gdańsk University of Technology, Narutowicza 11/12, 80-233 Gdańsk, Poland.

[b] Laboratory for High Performance Ceramics, Empa, Swiss Federal Laboratories for Materials Science & Technology, CH-8600 Dübendorf, Switzerland

[c] Laboratory of Inorganic Chemistry, Department of Chemistry and Applied Biosciences, ETH Zürich, CH-8093 Zürich, Switzerland

[d] Laboratory for Thin Films and Photovoltaics, Empa, Swiss Federal Laboratories for Materials Science & Technology, CH-8600 Dübendorf, Switzerland

[e] Faculty of Chemistry, Nicolaus Copernicus University in Torun, 87-100 Toruń, Poland

Corresponding authors:

*Gurdial Blugan, Laboratory for High-Performance Ceramics, Empa, Swiss Federal Laboratories for Materials Science & Technology, CH-8600 Dübendorf, Switzerland, e-mail: Gurdial.Blugan@empa.ch

*Monika Wilamowska-Zawłocka, Department of Energy Conversion and Storage, Faculty of Chemistry, Gdańsk University of Technology, Narutowicza 11/12, 80-233 Gdańsk, Poland, e-mail: monika.wilamowska@pg.edu.pl

Supporting information for this article is given via a link at the end of the document.

‡ These authors contributed equally.

KEYWORDS

Li-ion battery, nanoparticles, photochemistry, silicon oxycarbide, tin.

ABSTRACT

In this work, we report an innovative and facile UV light-assisted synthesis of a nanocomposite based on silicon oxycarbide (SiOC) and tin nanoparticles. SiOC ceramic matrix, containing a conductive free carbon phase, participates in lithium-ion storage, and buffers the volume changes of Li-alloying/de-alloying material. The reported synthesis procedure through a polymer-derived ceramic route involves the preparation of a single-source precursor by UV crosslinking of a preceramic polymer in the presence of a tin precursor. Pyrolysis of this starting precursor at 1000°C leads to a homogenous distribution of tin nanoparticles (25-35 nm) within the SiOC ceramic matrix, which is crucial for electrochemical stability of the material. SiOC/Sn nanocomposite tested as an anode for Li-ion battery exhibits high reversible capacity values (603 mAh g^{-1} at the current density of 74.4 mA g^{-1}), outstanding rate capability (524 mAh g^{-1} at 2232 mA g^{-1}), and superior stability (494 mAh g^{-1} after 250 charge/discharge cycles).

1. Introduction

The demand for high-performance lithium-ion batteries and the limitations of the most commonly used anode material, graphite, draw attention to the development of high-capacity alternatives. Tin is considered as one of the most promising materials owing to its excellent properties, such as *i)* the high gravimetric capacity of 994 mAh g^{-1}, *ii)* one of the highest volumetric capacities of ~2111 mAh cm^{-3} (in the fully lithiated state), arising from creating various binary phases, up to $Li_{22}Sn_5$ [1,2], and *iii)* relatively low lithiation potential of 0.6 V vs Li/Li^+ [3]. However, due to considerable volume changes upon lithiation/delithiation processes (>260%), tin has to be utilized in the form of nanoparticles or as dispersed in a matrix, which prevents agglomeration and maintains electrical contact upon volumetric changes [3,4]. Considering those criteria, various nano-tin composites have been tested, based on *i)* inactive-matrices like Fe [5], Cu [6] or Li_2O [7], *ii)* active-matrices, e.g. Sb [8], Al [9], polymer-derived ceramics [10,11] and *iii)* carbon [12–19] i.e. amorphous carbon [12], carbon coating [13,14], porous carbon [15], Sn/C encapsulated carbon nanofibers [16], Sn-filled carbon nanotubes [17]. Creating composites with tin nanoparticles overcomes, to some extent, the problem of volume expansion. However, composites often suffer from limited cycling stability, resulting in a fast capacity drop, relatively low capacity because of limited lithium diffusion or poor rate capability [5,15,18]. Among carbon-based composites, hollow carbon fibers or CNTs filled with tin nanoparticles exhibit outstanding electrochemical performance; unfortunately, the price of these composites is a serious obstacle. Also, the practice of a multi-stage synthesis route requires sophisticated equipment, making it too complicated for an industrial application [18].

Encapsulation of tin nanoparticles within a silicon oxycarbide (SiOC) ceramic matrix is an attractive and economical option for the realization of high capacities and cycling stabilities [10,11,20]. Polymer-derived SiOC ceramics are amorphous structures consisting of mixed bonds of silicon tetrahedra and carbon (SiO_xC_y (x,y = 0-4)), along with a free carbon phase interlacing the ceramic part, providing sufficient electrical conductivity [21–25]. SiOC is an attractive matrix for alloying nanoparticles due to its electrochemical activity towards Li-ions, providing high capacity values (500-600 mAh g^{-1}) [26,27], chemical stability and low

volume changes of the ceramic upon lithiation [28]. Moreover, the interconnected free carbon phase leads to softening of SiOC, which helps to accommodate volume changes upon the creation of Li-alloys [11,29–31]. SiOCs can be prepared by simple liquid routes, such as sol-gel or hydrosilylation, which enable the facile addition of new components. Composition and microstructure of SiOC can be easily tailored by appropriate selection of starting polymer precursors as well as synthesis and processing conditions [32–39].

SiOCs have already been tested as a matrix for tin nanoparticles. Tolosa et al. [40] created SiOC/Sn fiber mat by electrospinning the mixture of preceramic precursor and tin acetate with high initial capacity, but the capacity faded with prolonged cycles. Kaspar et al. [11] tested SiOCs with different carbon content as a potential matrix for tin nanoparticles. They reported composites with high capacity and stability, but these materials had reduced rate capability. Recently, Dubey et al. [10] made progress in terms of preceramic and tin precursor matching, achieving high capacity, good rate capability and good cycling stability.

The introduction of metallic tin nanoparticles into the ceramic material is typically performed through the mixing of a liquid preceramic polymer with tin-precursors [10,11,40]. The material is initially crosslinked to obtain a green body, and later pyrolyzed at elevated temperatures to get the final ceramic nanocomposite. During the pyrolysis, polymer-to-ceramic transformation and the carbothermal reduction of tin oxide (derived from tin precursor) leads to the generation and uniform distribution of tin nanoparticles within the ceramic matrix. However, carbothermal reduction consumes a part of free carbon, vital to provide sufficient conductivity and material softness. Thus, to achieve excellent electrochemical performance of SiOC/Sn composite, it is necessary to go for a preceramic polymer that leads to a carbon-rich ceramic composite [10,11].

One of the highest free carbon content in these ceramics, over 80 mol%, was reported for RD-684 polymer [11,39,41–43]. The RD-684 is a methylvinylphenyl polysiloxane resin, currently commercially available from Starfire Systems as SPR-684 Polyramic®. The resin can be cured in multiple ways, including thermal crosslinking [39,44,45], hydrosilylation [46,47], and photocrosslinking [41,48]. The last one is often realized by a simple UV (365 nm) irradiation process. In contrast to other methods, photocuring is very fast, single step and can be easily scaled up. In addition, it allows for the formation of dense and crack-free parts of various sizes and shapes [41,48]. Thus, applying the photocrosslinking method for producing SPR-684/Sn anodes may be an interesting option for modern high-performance Li-ion batteries. However, correct matching between the resin, photoinitiator, tin source, and other additives has to be made beforehand to ensure the generation and uniform distribution of metal nanoparticles within the matrix [49].

In this work, we explored the potential of SiOC/Sn composite derived from a combination of methylvinylphenyl polysiloxane and tin octoate precursors using photocrosslinking method for Li-ion battery's anode application. In our system, tin octoate ($Sn(Oct)_2$) is used as a tin source for two reasons: it mixes well with SPR-684 resin and other components, and its UV absorption maxima are in the range of 200-254 nm [50], which does not interfere with our UV source (365 nm). Furthermore, we added 1,4-butanediol diacrylate in order to: *i)* increase the crosslinking degree [51], *ii)* add an extra source of carbon, and *iii)* lower the viscosity of the synthesis mixture. The obtained SiOC/Sn nanocomposite exhibited a high capacity of 950 mAh g^{-1} in 5 mV-3 V potential range (600 mAh g^{-1} for 5 mV-1.5 V), excellent stability and good rate capability.

2. Materials and Methods

Reagents: Polyramic® SPR-684 polymer ($[-Si(C_5H_6)_2O-]_3[-Si(CH_3)(H)O-]_2[-Si(CH_3)(CH=CH_2)O-]_2$) was obtained from Starfire Systems, Inc (USA). Photoinitiator Genocure* LTM was obtained from Rahn AG (Switzerland). 1,4-Butanediol diacrylate (BDDA) and tin octoate were purchased from Sigma Aldrich (Switzerland). All materials were used as received.

SiOC/Sn composite synthesis: First, the preceramic mixture was prepared by combining 3.4 g of SPR-684 with 0.6 g of 1,4-butanediol diacrylate (85 : 15 wt% ratio). After a couple of minutes of mixing, 0.08 g photoinitiator and 2.67 g tin (II) ethylhexanoate were added to preceramic mixture (2 and 40 wt% of preceramic mixture, respectively). The mixture was stirred for 15 min at 400 rpm to obtain a homogeneous solution. Afterwards, the solution was uniformly distributed onto a Petri dish and crosslinked under a UV light (UV curing chamber, 365 nm) for 30 min. Then, the material was removed from the Petri dish, washed using acetone and ethanol and finally dried in an oven at 80°C for 48 h.

To obtain the final ceramic composite, the preceramic green body was pyrolyzed in a tubular furnace (Type 16-610, Carbolite GmbH, Germany) under controlled argon atmosphere using the following program: ramping to 250°C with a rate of 100°C h^{-1}, dwell at 250°C for 2 h, ramping to 1000°C with a rate of 150°C h^{-1}, dwell at 1000°C for 1 h, cooling to room temperature with a rate of 60°C h^{-1}. A schematic representation of the synthesis procedure is shown in **Figure S1** in Electronic Supplementary Information (ESI). The reference sample - pure SiOC ceramic - was also prepared using a similar method, but without addition of tin precursor.

Material characterization: The elemental contents of Sn, C and O in the samples (crushed into powders) were determined by elemental analysis performed by the company Mikroanalytisches Labor Pascher (Remagen-Bandorf, Germany). The content of Si was estimated as the difference between the total amount of all elements (100 wt%) and the sum of Sn, C and O contents, assuming a negligible amount of hydrogen in the samples. Thermal gravimetric analysis conjugated with differential scanning calorimetry (TGA-DSC) was performed on a Netzsch STA449 F3 Jupiter instrument under an argon atmosphere. Micro-Raman spectra in the range of 100-3200 cm^{-1} were obtained using a confocal micro-Raman spectrometer (In-Via, Renishaw, Wotton-under-Edge, UK) with an argon ion laser (514 nm). The spectra were analyzed with the aid of OriginPro2016 software. First, the background was subtracted using custom settings, then bands were fitted using Lorentzian peaks for D1, D2, D4, and G bands and Gaussian peak for D3 band, according to Sadezky et al. [52] Magic angle spinning nuclear magnetic resonance (MAS NMR) measurements for silicon ^{29}Si was performed on the Bruker Avance Ultrashield 500 MHz spectrometer with the following parameters: single pulse sequence, ^{29}Si frequency: 139.11 MHz, $\pi/8$ pulse length: 2.5 ms, recycle delay: 100 s, 1 k scans, external secondary reference: DSS. 3.2 mm zirconia rotors filled with samples were spun at 8 kHz under air flow. ^{29}Si NMR spectra were analyzed and deconvoluted using TopSpin software. FT-IR spectra were obtained from a Tensor 27, Bruker (Massachusetts, USA) using a Golden-Gate ATR. X-ray diffraction reflexes were recorded using X'Pert Pro MPD, PANalytical (Netherlands).The morphology and selected area electron diffraction (SAED) were characterized by transmission electron microscope (TEM by FEI, G2 F20X-Twin 200 kV, FEG). Energy-dispersive X-ray spectroscopy (EDS) by EDAX, RTEM model SN9577, 134 eV and parallel electron energy loss spectroscopy (PEELS) by Gatan Image Filter (GIF) spectra were recorded in order to identify the chemical elements and to show maps of elements in the selected areas. Measurements were performed in TEM mode (bright-field) and STEM mode (HAADF and EDX detectors). The samples were prepared for TEM measurements with the following procedure: a few milligrams of the sample were dispersed in etha-

nol (99.8% anhydrous) with the aid of ultrasonic dispersion for 5 s, then a drop of the dispersion (5 µL) was applied on carbon-coated copper mesh (Lacey type Cu 400 mesh, Plano) and left at room temperature for evaporation of the solvent.

Electrochemical measurements: Pyrolysed materials were initially ground in agate mortar to obtain median particle size D90 below 40 µm. Active materials (SiOC 85 wt%, carbon black (CB, Super P, TIMCAL, Switzerland), 7.5 wt%) were ball-milled in a planetary ball-mill at 350 rpm for 30 min. 7.5 wt% of carboxymethyl cellulose (CMC, SUNROSE MAC 500LC, Nippon Paper Group) was added to the SiOC/carbon black mixture, and the mixture was subjected to planetary ball-milling at 350 rpm for 1 h. The obtained slurry was coated on a Cu-foil using a doctor-blade and later dried overnight in a vacuum oven at 120°C. Electrode material loadings were in the range of 2-3 mg cm^{-2}. Test cells were assembled using stainless-steel coin-type cells (CR2025) in a glovebox under an inert Ar atmosphere (<0.1 ppm H_2O/O_2) with a glass microfiber separator and 130 µL of 1 M $LiPF_6$ (battery grade, Novolyte Technologies), in 1:1 by weight mixture of EC:DMC (ethylene carbonate (EC, battery grade, BASF), dimethyl carbonate (DMC (battery grade, BASF)) with 3 wt% FEC (fluoroethylene carbonate (FEC, >98%, TCI Chemicals)). The diameter of the electrodes was 12 mm. The coin cells were electrochemically cycled using a multichannel electrochemical workstation (Astrol BAT-Flex) after a waiting time of 2 h.

Electrochemical measurements were performed on a multichannel workstation (MPG-2, Bio-Logic SAS) and on the Biologic Potentiostat SP200 (BioLogic Science Instruments, Seyssinet-Pariset, France). Galvanostatic charge/discharge was performed in the potential range of 0.005 V and 1.5 V vs. Li/Li^+ at various currents (the same for charge and discharge $I_{charge} = I_{discharge}$). Cyclic voltammetry was recorded within the same potential range with the scan rate of 0.1 and 1 mV s^{-1}. Electrochemical impedance spectroscopy measurements were performed in the frequency range from 100 kHz to 10 mHz with the amplitude equal to 5 mV. EIS spectra were recorded at a rest potential equal to 3 V for the fresh (not lithiated) electrode and 0.15 V for the lithiated electrodes.

3. Results and Discussion

The results of elemental analysis of SiOC and SiOC/Sn samples are presented in **Table 1**. The elemental composition of pure SiOC ceramic is similar to the previously reported values [11,39,41–43]. The pure ceramic contains 48 wt% of carbon, which classifies this SiOC into C-rich category. The weight ratio between ceramic and free carbon phase in SPR-684 based SiOC was determined as 56:44, which is an optimal value to achieve good electrochemical performance [10,27,53]. In the SiOC/Sn composite, the amount of carbon is significantly lower (22.6 vs. 48.3 wt% in pure SiOC) due to carbothermal reduction of tin oxides (created upon decomposition of tin precursor) at elevated temperature, which generates metallic tin (20.7 wt%). Ceramic matrix content is slightly higher in SiOC/Sn composite (60.7 wt% compared to 56 wt% for pure SiOC). The Si:O ratio changes from 1.33 for SiOC to 1.24 for SiOC/Sn. Higher amounts of oxygen in SiOC/Sn composite may be explained by consumption of carbon and possible oxidation of Si during the carbothermal reduction process [40].

Table 1. Elemental composition of SiOC/Sn and SiOC samples.

Sample	Elemental content (wt%)				$SiC_xO_{2(1-x)}$	C_{free}	Wt% C_{Free}	Wt% SiOC	Wt% Sn
	Si	C	O	Sn					

SiOC/Sn	31.39	22.61	25.30	20.70	$SiC_{0.29}O_{1.41}$	1.39	18.64	60.66	20.70
SiOC	29.56	48.34	22.10	0	$SiC_{0.34}O_{1.31}$	3.47	43.96	56.04	0.00

The crosslinking process of the pure precursor and the precursor mixed with the tin source was tracked by means of FT IR spectroscopy. **Figure 1a** shows FT IR spectra for SPR-684 precursor and the green body samples before pyrolysis (denoted as SiOC-Pre and SiOC/Sn-Pre).

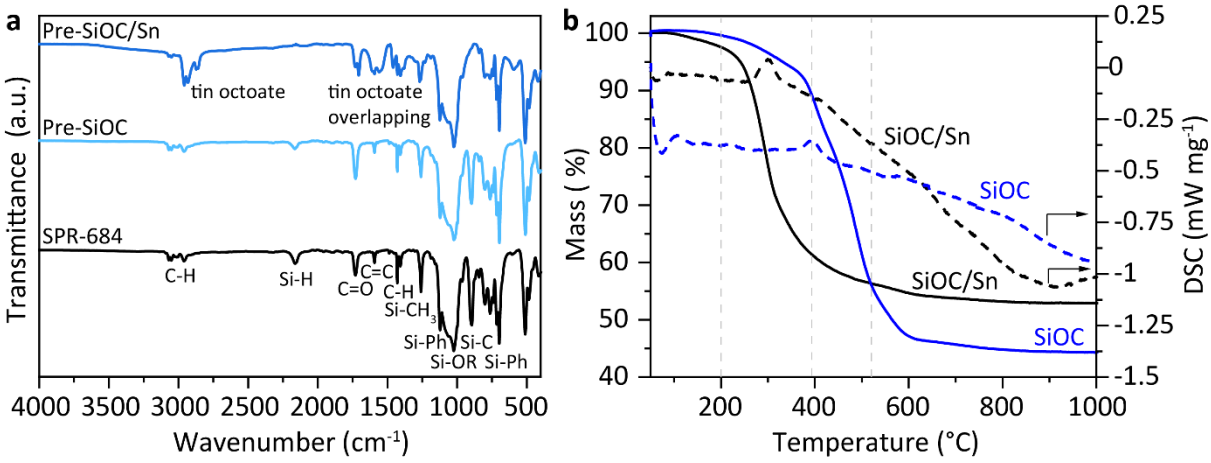

Figure 1. a) FTIR of the preceramic precursor SPR-684, and the green bodies of the pure preceramic (SiOC-Pre) and nanocomposite (SiOC/Sn-Pre) samples; **b**) TGA and DSC of SiOC and SiOC/Sn samples.

The SPR-684 polymer spectra reveal a number of bands, which may be attributed to the vibration of the following bonds: ~2950 (m) cm^{-1} (C-H), ~2150 (m-s) cm^{-1} (Si-H), ~1730 (s) cm^{-1} (C=O), ~1592 (s) cm^{-1} (C=C), ~1024 (vs) cm^{-1} (Si-OR), and ~892 (m-s) cm^{-1} (Si-C and/or Si-H) [32,54]. Crosslinking of the SPR-684 polymer with BDDA (SiOC-Pre sample) occurs via reactions between C=C groups as well as between Si-H and C=C bonds [41]. Photocrosslinked Pre-SiOC sample exhibits: *i)* the increase of the absorption at ~1730 cm^{-1}, which is directly related to the introduction of new C=O bonds coming from BDDA, *ii)* the decrease of the band at ~1592 cm^{-1} related –C=C– bonds, and *iii)* the decrease of the band corresponding to Si-H. These changes confirm the creation of crosslinks between SPR-684 chains and BDDA [51]. In the case of SiOC/Sn-Pre sample, additional bands in the range of 2800-2995 cm^{-1} and 1750-1100 cm^{-1} appeared, which is directly related to the introduction of tin (II) octoate [55]. Deformation vibrations of Si–H bonds, coming from the SPR-684 polymer, disappeared in the spectrum of the blend with tin precursor (SiOC/Sn-Pre), which suggests that the presence of metal (from tin (II) octoate) may catalyze reactions between Si–H and –C=C– such as dehydrocoupling and/or hydrosilylation as reported in the literature [56–58].

The pyrolysis process was examined through TGA-DSC analysis (**Figure 1b**). For the SiOC/Sn sample, mass loss started at a lower temperature (approx. 80°C compared to 140°C for pure SiOC). These slow gradual losses at lower temperatures can be related to the evaporation of unreacted substrates (e.g. BDDA in the case of SiOC sample and BDDA and tin octoate in the case of SiOC/Sn sample) or residues of solvents after washing procedures [59]. The starting small mass loss at low temperatures is more pronounced for the composite, because the molecular mass of tin octoate is much higher than BDDA (405.12 vs 198.22 g mol^{-}

[1]). Above 230°C, a substantial mass loss is noticed for SiOC/Sn, which is connected with the decomposition of tin octoate. The DSC peak at ~290 °C, corresponding to the thermal degradation of tin octoate, confirms the release of volatile products from the sample. At higher temperatures, the weight loss may be assigned to the carbothermal reduction of tin octoate in SiOC/Sn sample as well as the decomposition and removal of organic functional groups and Si-bonds rearranging in both samples [59,60]. The temperatures of the thermal conversion of the preceramic polymer are also confirmed by TGA of the pure SPR-684 polymer, (**Figure S2** in ESI), which reveals a substantial mass loss in the temperature range of 400 – 600°C. The DSC peak at ~394°C, observed only for the SiOC sample, may be related to the thermal decomposition of acrylates [61] and/or thermal degradation of poorly crosslinked polysiloxanes [62]. The lack of this peak for the SiOC/Sn nanocomposite may be rationalized by a higher crosslinking degree compared to the pure SiOC as indicated by chances of metal catalyzed crosslinking of polymer networks (FTIR). This may be another reason, besides the high molecular mass of tin, of a lower weight loss for SiOC/Sn sample (47%) compared to SiOC (56%). The TGA results show that the polymer to ceramic conversion occurs at lower temperatures for SiOC/Sn nanocomposite (up to approx. 500°C) compared to the pure SiOC (~600°C).

To track the completion of the carbothermal reduction, XRD measurements were conducted. XRD spectra for SiOC and SiOC/Sn samples are presented in **Figure 2**. The pure SiOC sample exhibits a characteristic halo at around 23° and a broad peak at 43°. Such a broad halo is typical for amorphous silica [63] as well as amorphous structure of SiOC [64,65]. The peak detected at around 43° is typical for dispersed graphene layers creating amorphous structure [39,66]. All the peaks registered for pure SiOC are very broad and non-distinctive. In contrast, SiOC/Sn composite exhibits a series of sharp, well-defined peaks, all related to the presence of tin with a tetragonal crystallographic structure, which in the literature [67,68] occurs as β-Sn with unit cell parameters of 0.595, 0.595, 0.321 nm. No peaks related to SnO_2 were recorded, suggesting the completion of carbothermal reduction.

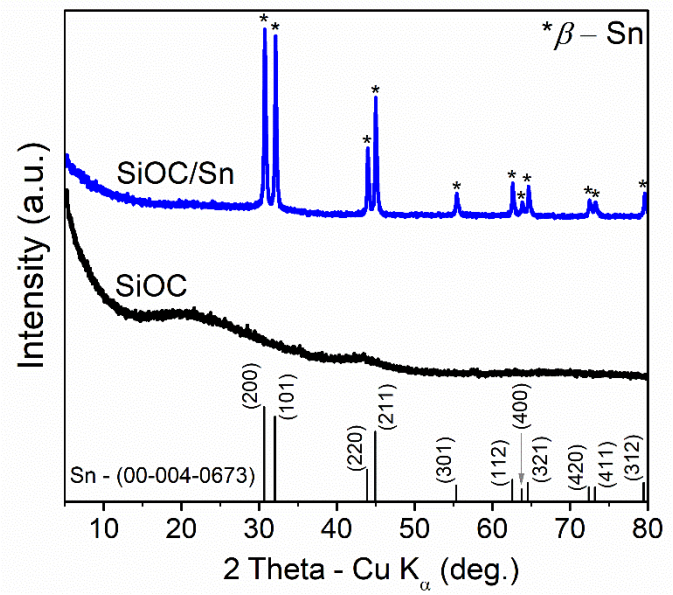

Figure 2. X-ray diffractograms of SiOC and SiOC/Sn samples. The powder diffraction file (PDF) reference β-Sn (00-004-0673) is given in the bottom.

A homogeneous material with an amorphous structure was observed in the TEM images of the SiOC sample (**Figure 3a-c**). These observations are confirmed by the diffraction pattern

(**Figure 3d**), characteristic of samples with a disordered structure. In the case of SiOC/Sn nanocomposite, two structures were observed in the subsequent TEM images (**Figure 3e-g**). The first is amorphous, the same as in the case of pure SiOC (**Figure 3a-c**), the second is crystalline, in the form of black spherical nanoparticles with a diameter of about 15 nm (**Figure 3g**). Both structures are confirmed by the diffraction pattern (**Figure 3h**), which shows white reflections symmetrically arranged on a circle. Based on the distances between the pairs of these reflections, the interplanar distances were determined to be 0.2764 and 0.2000 nm. Both values match into a tetragonal tin structure (see Table S2 in ESI for distances {101} and {220}) and confirm the presence of highly crystalline β-Sn nanoparticles [10,68,69]

The STEM images of SiOC/Sn show bright areas surrounded by a darker material. (**Figure 4a-b**). The properties of the HAADF detector show that the round, brighter areas contain elements with a greater atomic number than the surroundings. These observations are confirmed by maps of the distribution of elements: carbon, oxygen, silicon, and tin. The presence of C, O, Si in the SiOC sample and additionally Sn in the SiOC/Sn nanocomposite was identified by this method. EDX spectra of these samples are presented in **Figure 4c-f** and in **Figure S3** (in ESI). Additional information on the Sn chemical state can be seen in the PEELS spectra presented for the SiOC/Sn nanocomposite (**Figure 4g and Figure S4** in ESI). The shape of the PEELS spectrum for tin with two peaks at 9 and 18 eV suggest that tin in the composite occurs only in the metallic form [70,71]. The results are consistent with XRD pattern (**Figure 2**), which exhibits Bragg peaks only for β-Sn.

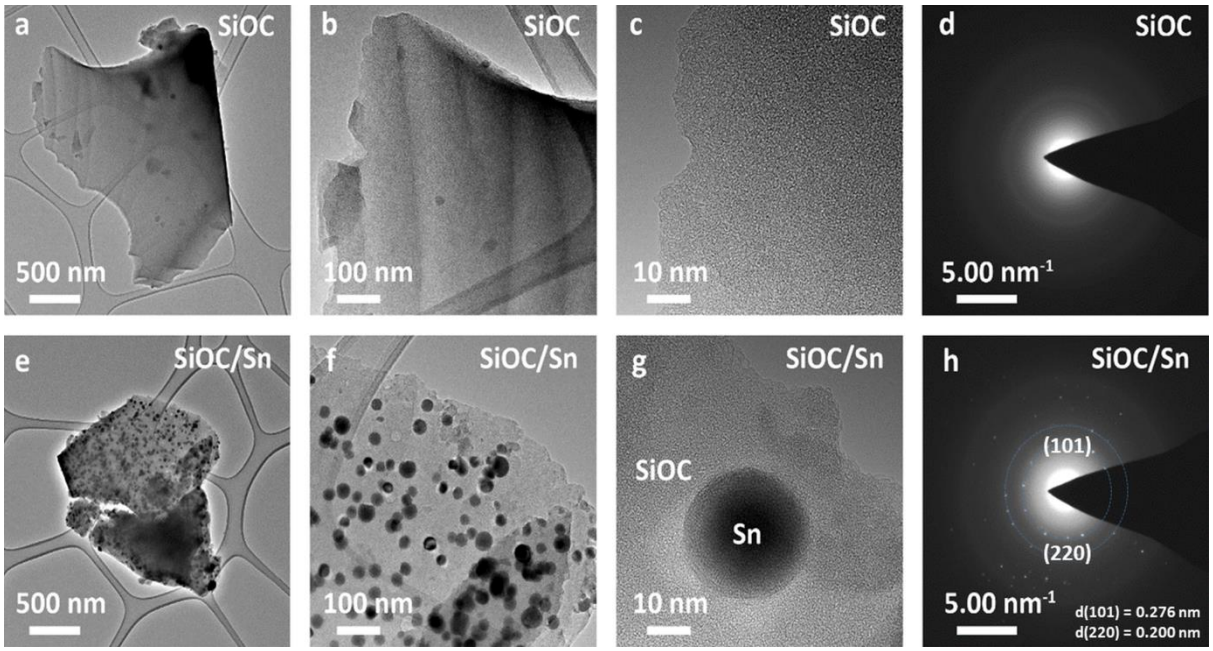

Figure 3. TEM images of SiOC (a-c) and SiOC/Sn (e-g) and the corresponding SAED patterns g) for SiOC and h) for SiOC/Sn.

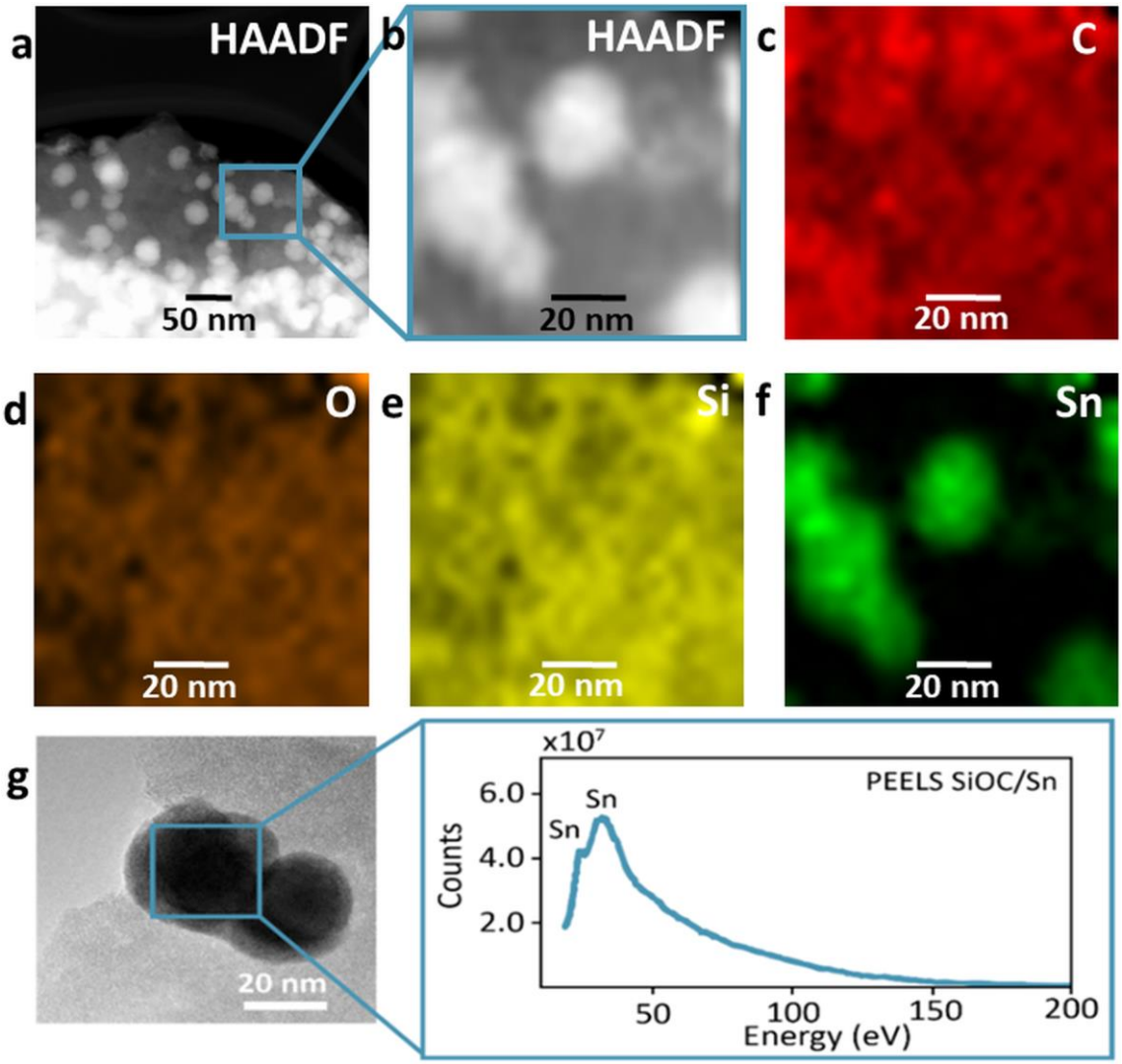

Figure 4. (**a,b**) HAADF-STEM image and (**c-f**) STEM-EDX mapping of SiOC/Sn samples, **g**) STEM-PEELS of SiOC/Sn nanocomposite.

The size distribution of tin nanoparticles is presented in **Figure S5** (in ESI). The distribution was made based on measurements of ~100 nanoparticles of tin. Their mean size was estimated as 30.35 ± 10.82 nm.

^{29}Si MAS NMR spectra of SiOC and SiOC/Sn samples (**Figure 5**) show the structure of the ceramic part. Pronounced changes are identified in the share of the silicon tetrahedra (SiO_4, SiO_3C, SiO_2C_2, $SiOC_3$ and SiC_4) between the pure ceramic and the nanocomposite with tin, as presented in **Table 2**. SiOC/Sn samples exhibit a significantly lower share of mixed silicon bonds, namely (SiO_3C, SiO_2C_2, $SiOC_3$, SiC_4), and higher content of amorphous silica (SiO_4). This may be explained by carbothermal reduction of SnO to metallic tin leading to oxidation of carbon and to some extent, also silicon atoms [40].

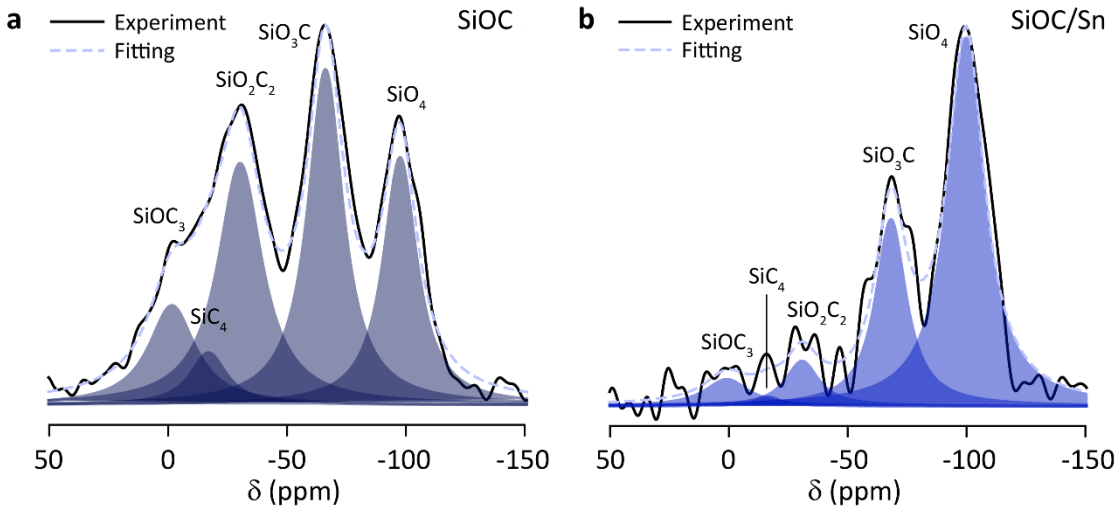

Figure 5. ^{29}Si MAS NMR spectra of a) SiOC and b) SiOC/Sn samples.

Table 2. Data from the deconvolution of 29Si MAS NMR spectra of SiOC/Sn and SiOC samples.

Sample	SiO_4		SiO_3C		SiO_2C_2		$SiOC_3$		SiC_4	
	δ / ppm	%	δ / ppm	%	δ / ppm	%	δ / ppm	%	δ / ppm	%
SiOC	-97.6	22.4	-66.2	31.8	-30.3	29.0	-1.6	12.3	-17.0	5.1
SiOC/Sn	-99.8	60.9	-68.2	26.0	-30.8	6.8	0.9	5.2	-16.7	1.1

To get information about free carbon phase evolution after addition of tin source, Raman spectra of the pyrolysed materials were acquired. **Figure 6a** shows Raman spectra of SiOC and SiOC/Sn samples. Both spectra overlap almost ideally, and their deconvolutions (**Figure 6b and c**, and **Table S1** in ESI) show minor changes in the component peaks. The deconvolution was performed according to Sadezky et al. [52] The results confirm that there are no significant differences in carbon structure between both materials. This suggests that the carbothermal reduction process does not disturb the structure of the free carbon phase, although it consumes carbon atoms in mixed bond silicon tetrahedra, as shown in ^{29}Si NMR spectra (**Figure 5**). The Raman spectra of SiOC/Sn exhibits a bit higher noise than the pure SiOC sample. This could be rationalized by a lower carbon content, as shown by elemental analysis.

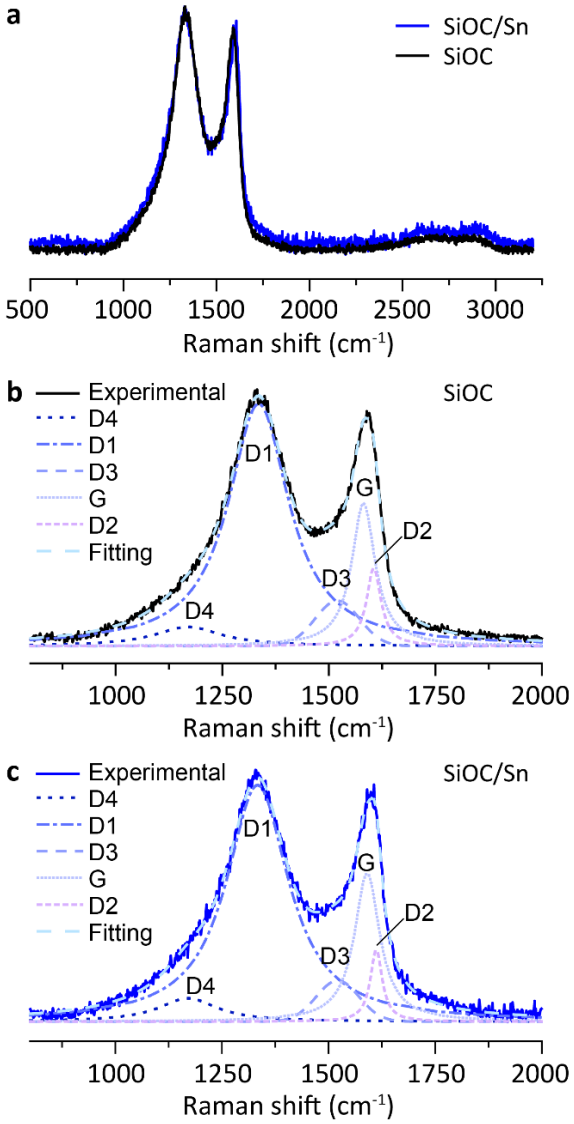

Figure 6. a) Comparison of Raman spectra of SiOC/Sn and SiOC samples; deconvolution of **b)** SiOC and **c)** SiOC/Sn Raman spectra.

To evaluate the electrochemical activity of tin nanoparticles in the ceramic matrix, cyclic voltammetry (CV) measurements were performed. **Figures 7a and b** present CV curves of pure SiOC and SiOC/Sn nanocomposite, respectively. On the cathodic site, pure SiOC ceramic exhibits gradual current rise starting at around 0.9 V, which represents the insertion of the lithium into the ceramic, while on the anodic side a broad halo, typical for carbon-rich SiOC, is observed [72]. SiOC/Sn nanocomposite in the first CV cycle presents gradual current rise on the cathodic site and two small broad peaks at 0.68 and 0.86 V on the anodic site. In the following cycles, two distinct reduction peaks appear, first around 0.56 V representing the creation of Li_2Sn_5 and second at around 0.25 V, which corresponds to various tin lithiation stages [11,73]. On the anodic side, two peaks become much more pronounced and slightly shifted towards higher potentials upon cycling. This gradual increase of oxidation and reduction currents suggests that the nanocomposite is slowly activated over the first few cycles, which may be connected with the creation of diffusion paths for lithium ions in the ceramic matrix. The redox peaks are more distinct for the slower scan rates, as presented in **Figure S7a** (in ESI).

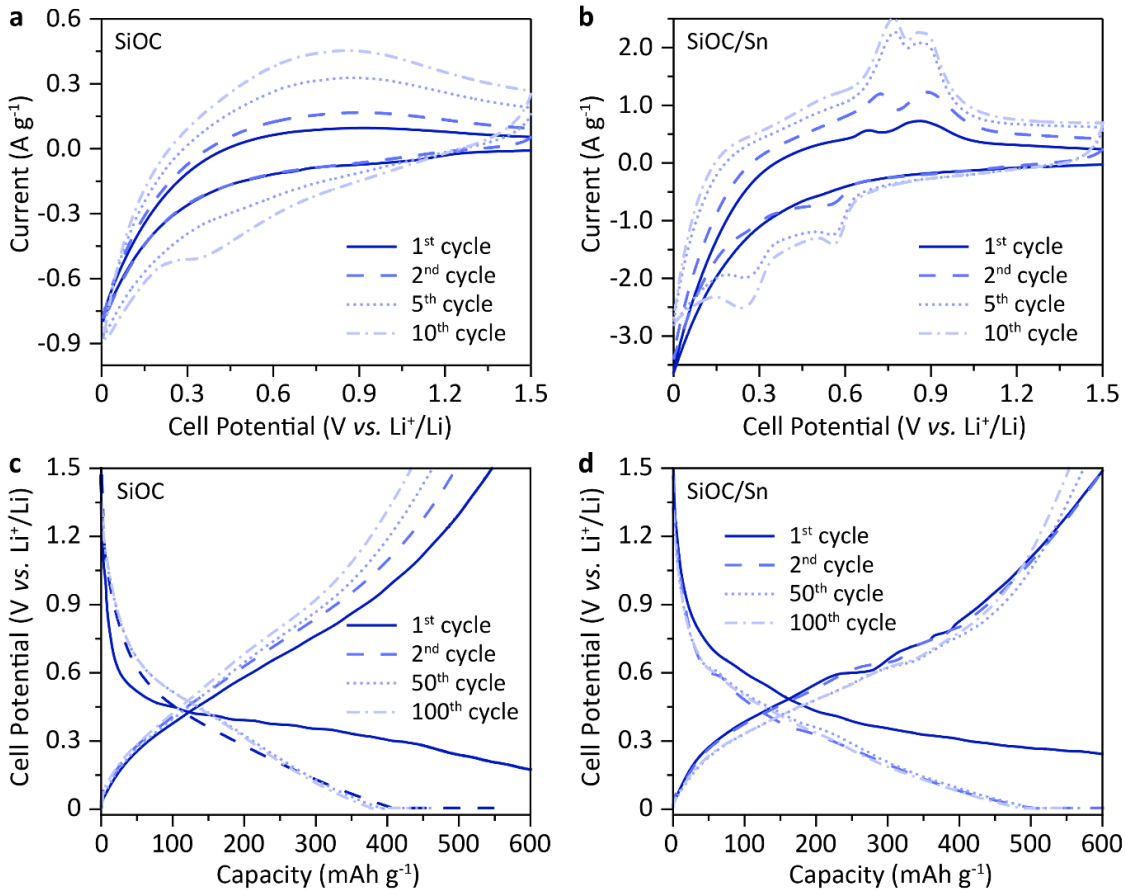

Figure 7. Cyclic voltammetry curves of **a**) pure SiOC and **b**) SiOC/Sn nanocomposite; scan rate 1 mV s^{-1}, electrolyte 1 M $LiPF_6$ (EC:DMC 1:1 v/v), half-cell configuration, Li-counter/reference electrode. Charge-discharge profiles for selected cycles of **c**) SiOC and **d**) SiOC/Sn samples, at 372 mA g^{-1}.

Galvanostatic charge-discharge profiles of the selected cycles for pure SiOC and SiOC/Sn are presented in **Figure 7c and d**, respectively. During the first lithiation step (solid line), the SiOC sample exhibits a rapid potential decrease followed by a long, smooth plateau-like curve, starting from approx. 0.5 V. This plateau indicates a gradual insertion of lithium ions, typical for SiOC ceramics, and corresponds well with the CV curve. Irreversibility of this plateau is connected with the creation of solid-electrolyte interphase (SEI) and irreversible bonding of lithium ions in oxygen-rich silicon tetrahedra [74]. In the case of SiOC/Sn samples, small and blurred plateaus on the lithiation and delithiation curves are observed between 0.9-0.4 V. These plateaus correspond to redox peaks in the CV curve and are related to alloying steps for tin nanoparticles [73]. The first delithiation capacity of the pure SiOC is equal to 546 mAh g^{-1}, and is slightly fading over subsequent cycles. The SiOC/Sn composite exhibits a higher initial reversible capacity of 603 mAh g^{-1} and better cycling stability as presented in **Table 3** and **Figure 8a**.

For the cycling stability tests, the materials were initially cycled once at 18.6 mA g^{-1} current rate to create a stable solid electrolyte interphase. The following cycles were recorded at 372 mA g^{-1} (1C in terms of graphite). The SiOC/Sn nanocomposite exhibits better capacity retention (82%) (calculated as a ratio between the 250th cycle reversible capacity (C_{rev}) to 1st cycle reversible capacity) compared to the pure SiOC (73%). Electrochemical impedance spectroscopy measurements performed during cycling test support the better stability of the composite compared to the pure ceramic. The Nyquist plots of the fresh (not lithiated), and

after 1st, 50th, 150th and 250th lithiation for SiOC and SiOC/Sn samples are presented in **Figure S6** (in ESI). The impedance spectra of the fresh sample, recorded at 3 V (vs Li/Li^+), exhibit a semicircle and straight capacitive line. The shapes are the same for both samples, the difference is in the value of charge transfer resistance, which is lower for the SiOC/Sn composite (approx. 35 Ω compared to ~55 Ω for the SiOC sample) due to the presence of metallic tin, which increases conductivity. After the first lithiation, the semicircle is higher than after the repetitive cycling, which means that the charge transfer resistance decreases upon cycling due to creation of lithium ion diffusion paths. This is the evidence of the good stability of both samples. In the case of SiOC/Sn sample the value of charge transfer resistance stabilizes after 50th cycle, whereas for SiOC slightly increases between 50th and 250th cycle. These results show that besides the repetitive alloying and de-alloying processes occurring in SiOC/Sn sample, it shows better stability than the pure SiOC.

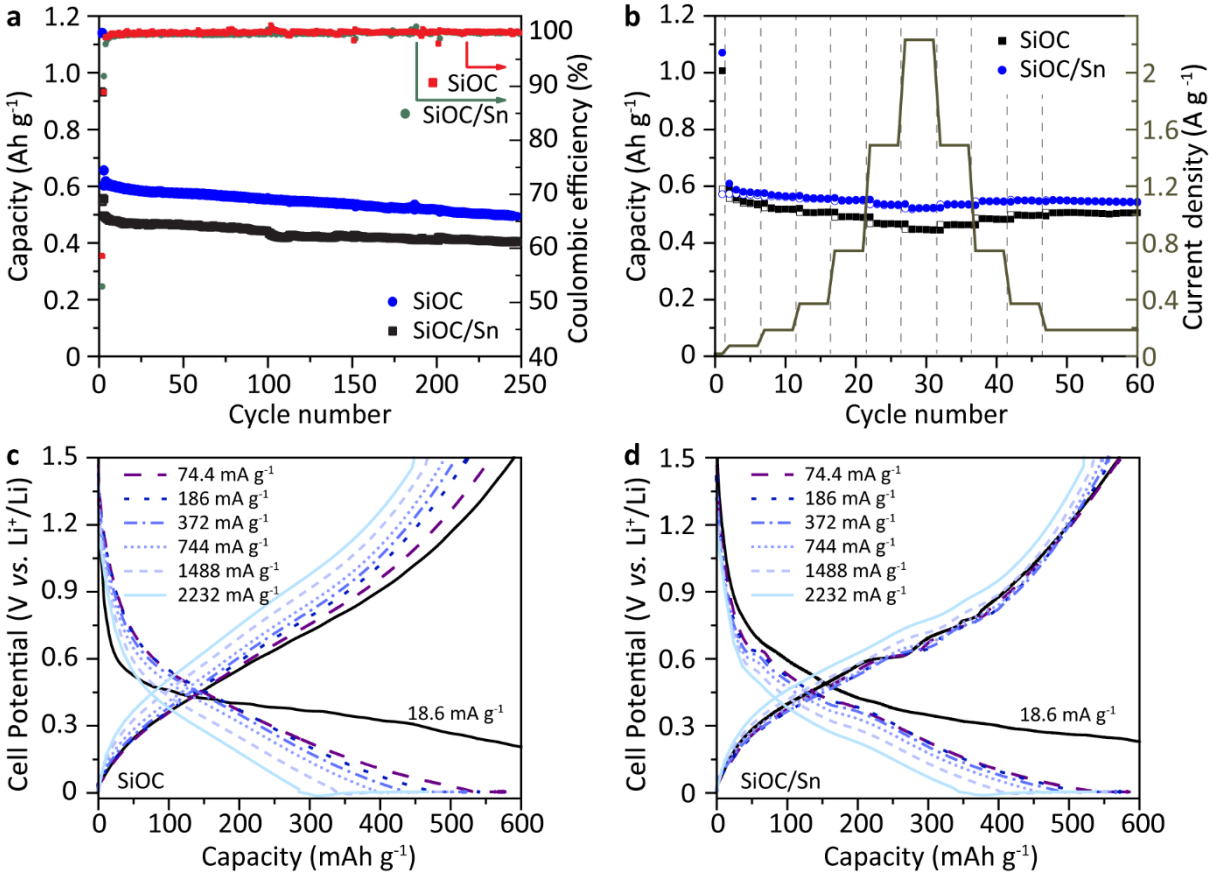

Figure. 8. **a**) Cycling performance of SiOC and SiOC/Sn samples at 372 mA g^{-1} and the corresponding Coulombic efficiency of each cycle, **b**) rate capability of SiOC and SiOC/Sn samples, current rates in the range of 18.6 and 2232 mA g^{-1} and the corresponding charge-discharge profiles of **c)** SiOC and **d)** SiOC/Sn.

Table 3. Irreversible capacity (C_{irrev}) of the 1st cycle (calculated as the difference between the first lithiation capacity and the first delithiation capacity), reversible delithiation capacity (C_{rev}) of the 1st and 250th cycle, Coulombic efficiency of the 1st cycle (η) and capacity retention of SiOC and SiOC/Sn samples. The capacity retention was calculated as a quotient of the 250th cycle C_{rev} to the 1st cycle C_{rev} (%)

Material	1st cycle	1st cycle	250th cycle	η / %	Capacity

	C_{irrev}/mAh g^{-1}	C_{rev}/mAh g^{-1}	C_{rev}/mAh g^{-1}		retention / %
SiOC	386	546	397	59	73
SiOC/Sn	537	603	494	53	82

One of the key parameters for commercial applications is a good rate capability of electrode materials. A comparison of the rate capability of the pure SiOC ceramic and the SiOC/Sn nanocomposite in the 5 mV - 1.5 V potential range (commercially useful region) is presented in **Figure 8b**. The corresponding charge-discharge profiles for each of the applied current rates are shown in **Figure 8c and d** for SiOC and SiOC/Sn, respectively. The SiOC/Sn nanocomposite shows a much smaller capacity decrease with increasing polarization current compared to the pure ceramic. The capacity regained at 2232 mA g^{-1} is equal to 450 and 524 mAh g^{-1} for SiOC and SiOC/Sn, respectively. This implies that the nanocomposite at 6C rate preserves 92% of the capacity achieved at C/5, while the pure SiOC retains 83%. After reducing the current rate back to the low values (74.4 mA g^{-1}), the capacity of both materials is almost fully recovered. Much higher capacity values, excellent capacity recovery at high current rates **(Figure S7b** in ESI) and good stability upon prolonged cycling (**Figure S7c and d** in ESI) was obtained in the full potential range (5 mV - 3 V). The capacity at 74.4 and 2232 mA g^{-1} current rate recorded for SiOC/Sn sample is over 1050 and 800 mAh g^{-1}, respectively. To give a perspective, Liang et al. [75] recently published a review paper presenting a general development of tin-based anodes. Comparing obtained capacity results to representative findings in various groups of tin-based materials (nano-, micro-tin alloys, tin oxides, tin/carbonaceous composites, contact type materials, elemental tin, etc.) our composite material exhibits one of the highest cyclic stability and rate capability. Still, the results must be treated with caution, since electrochemical response may vary depending on multiple conditions [76]. Nevertheless, considering high capacity values, excellent cyclic stability and rate capability together with relatively easy and cheap preparation process, our SiOC/Sn nanocomposite is a prospective anode Li-ion battery.

4. Conclusions

In this work, we present a new method for the synthesis of SiOC/Sn composite as anode material for Li-ion batteries. The composite was prepared from a commercially available polysiloxane resin and a tin precursor by a simple UV-irradiation process followed by pyrolysis under an inert atmosphere at 1000°C. We show that UV-irradiation process in the presence of tin octoate leads to a dual photocuring-dehydrocoupling/hydrosilylation crosslinking mechanism resulting in a lower weight loss during pyrolysis and better preservation of ceramic matrix. The described process leads to a homogenous distribution of metallic tin in the form of nanoparticles (25-35 nm) within the ceramic matrix. The utilization of carbon-rich preceramic precursor allowed for the preservation of sufficient amount of free carbon, necessary to achieve high stability and good conductivity. The obtained SiOC/Sn nanocomposite exhibits high capacity of 494 mAh g^{-1} after 250 charge/discharge cycles and excellent rate capability with capacity of 524 mAh g^{-1} at 2.3 A g^{-1}, all values measured in the 0-1.5 V potential range. Outstanding electrochemical performance and simple preparation procedure give a high potential for this SiOC/Sn nanocomposite material in Li-ion battery applications.

5. Acknowledgements

D.K. acknowledges the support from European Social Fund, project "The development of an interdisciplinary and international PhD study programmes" InterPhD2, project no. POWR.03.02.00-00-I002/16. M.W.Z. acknowledges the support of Foundation for Polish Science (HOMING PLUS/2012-6/16).

6. Funding

P.V.W.S. acknowledges the funding from the EMPAPOSTDOCS-II program. The EMPAPOSTDOCS-II program has received funding from the European Union's Horizon 2020 Research and Innovation Program under the Marie Skłodowska-Curie grant agreement number 754364.

7. CRediT authorship contribution statement:

D.K.: Investigation, Formal analysis, Data Curation, Visualization, Writing – Original Draft; **P.V.W.S**.: Conceptualization, Methodology, Formal Analysis, Writing – Original draft, Review & Editing, Supervision; **R.D.**: Investigation, Visualization, Writing – Review & Editing, **M.A.:** Investigation, Formal Analysis, **K.V.K.**: Writing – Review & Editing, **G.T.**: Investigation, Visualization, Writing – Original Draft, **M.V.K.**: Writing – Review & Editing, **T.G.**: Writing – Review & Editing, Resources, **M.W.Z.**: Formal Analysis, Visualization, Supervision, Writing – Original Draft, Review & Editing, **G.B.**: Writing – Review & Editing, Funding Acquisition

8. Data availability

Data available on request from the authors.

9. References:

[1] M.N. Obrovac, V.L. Chevrier, Alloy Negative Electrodes for Li-Ion Batteries, Chem. Rev. 114 (2014) 11444−11502. doi:dx.doi.org/10.1021/cr500207g.

[2] C.M. Park, J.H. Kim, H. Kim, H.J. Sohn, Li-alloy based anode materials for Li secondary batteries, Chem. Soc. Rev. 39 (2010) 3115–3141. doi:10.1039/b919877f.

[3] B. Scrosati, J. Hassoun, Y.-K. Sun, Lithium-ion batteries. A look into the future, Energy Environ. Sci. 4 (2011) 3287–3295. doi:10.1039/c1ee01388b.

[4] I.A. Courtney, W.R. McKinnon, J.R. Dahn, On the Aggregation of Tin in SnO Composite Glasses Caused by the Reversible Reaction with Lithium, J. Electrochem. Soc. 146 (1999) 59–68. doi:10.1149/1.1391565.

[5] O. Mao, J.R. Dahn, Mechanically Alloyed Sn-Fe(-C) Powders as Anode Materials for Li-Ion Batteries: II. The Sn-Fe System, J. Electrochem. Soc. 146 (1999) 405–413. doi:10.1149/1.1391623.

[6] N. Tamura, R. Ohshita, M. Fujimoto, S. Fujitani, M. Kamino, I. Yonezu, Study on the anode behavior of Sn and Sn-Cu alloy thin-film electrodes, J. Power Sources. 107 (2002) 48–55. doi:10.1016/S0378-7753(01)00979-X.

[7] D.L. Foster, J. Wolfenstine, J.R. Read, W.K. Behl, Nanocomposites of Sn and Li_2O formed from the chemical reduction of SnO as negative electrode material for lithium-ion batteries, Electrochem. Solid-State Lett. 3 (2000) 203–204.

doi:10.1149/1.1391002.
[8] J. Hassoun, G. Derrien, S. Panero, B. Scrosati, A SnSb-C nanocomposite as high performance electrode for lithium ion batteries, Electrochim. Acta. 54 (2009) 4441–4444. doi:10.1016/j.electacta.2009.03.027.
[9] R.Z. Hu, L. Zhang, X. Liu, M.Q. Zeng, M. Zhu, Investigation of immiscible alloy system of Al-Sn thin films as anodes for lithium ion batteries, Electrochem. Commun. 10 (2008) 1109–1112. doi:10.1016/j.elecom.2008.05.012.
[10] R.J.-C. Dubey, P.V.W. Sasikumar, F. Krumeich, G. Blugan, J. Kuebler, K. V. Kravchyk, T. Graule, M. V. Kovalenko, Silicon Oxycarbide—Tin Nanocomposite as a High-Power-Density Anode for Li-Ion Batteries, Adv. Sci. (2019) 1901220. doi:10.1002/advs.201901220.
[11] J. Kaspar, C. Terzioglu, E. Ionescu, M. Graczyk-Zajac, S. Hapis, H.J. Kleebe, R. Riedel, Stable SiOC/Sn nanocomposite anodes for lithium-ion batteries with outstanding cycling stability, Adv. Funct. Mater. 24 (2014) 4097–4104. doi:10.1002/adfm.201303828.
[12] G. Derrien, J. Hassoun, S. Panero, B. Scrosati, Nanostructured Sn-C composite as an advanced anode material in high-performance lithium-ion batteries, Adv. Mater. 19 (2007) 2336–2340. doi:10.1002/adma.200700748.
[13] J.S. Choi, Y.J. Lee, H.J. Lee, G.B. Cho, J.W. Byeon, H.J. Ahn, K.W. Kim, J.H. Ahn, K.K. Cho, Optimization of carbon coating thickness to prevent crack generation in Sn nanoparticles during charge/discharge process and their electrochemical properties, J. Alloys Compd. 843 (2020) 155892. doi:10.1016/j.jallcom.2020.155892.
[14] Y. Xu, Q. Liu, Y. Zhu, Y. Liu, A. Langrock, M.R. Zachariah, C. Wang, Uniform nano-Sn/C composite anodes for lithium ion batteries, Nano Lett. 13 (2013) 470–474. doi:10.1021/nl303823k.
[15] Y. Xu, Y. Zhu, Y. Liu, C. Wang, Electrochemical performance of porous carbon/tin composite anodes for sodium-ion and lithium-ion batteries, Adv. Energy Mater. 3 (2013) 128–133. doi:10.1002/aenm.201200346.
[16] Y. Yu, L. Gu, C. Wang, A. Dhanabalan, P.A. Van Aken, J. Maier, Encapsulation of Sn@carbon nanoparticles in bamboo-like hollow carbon nanofibers as an anode material in lithium-based batteries, Angew. Chemie - Int. Ed. 48 (2009) 6485–6489. doi:10.1002/anie.200901723.
[17] T.P. Kumar, R. Ramesh, Y.Y. Lin, G.T.K. Fey, Tin-filled carbon nanotubes as insertion anode materials for lithium-ion batteries, Electrochem. Commun. 6 (2004) 520–525. doi:10.1016/j.elecom.2004.03.009.
[18] A.R. Kamali, D.J. Fray, Tin-based materials as advanced anode materials for lithium ion batteries: A review, Rev. Adv. Mater. Sci. 27 (2011) 14–24.
[19] A.P. Nowak, K. Trzciński, M. Szkoda, G. Trykowski, M. Gazda, J. Karczewski, M. Łapiński, D. Maskowicz, M. Sawczak, A. Lisowska-Oleksiak, Nano Tin/Tin Oxide Attached onto Graphene Oxide Skeleton as a Fluorine Free Anode Material for Lithium-Ion Batteries, Inorg. Chem. 59 (2020) 4150–4159. doi:10.1021/acs.inorgchem.0c00318.
[20] Z. Liu, Q. Yu, Y. Zhao, R. He, M. Xu, S. Feng, S. Li, L. Zhou, L. Mai, Silicon oxides: A promising family of anode materials for lithium-ion batteries, Chem. Soc. Rev. 48 (2019) 285–309. doi:10.1039/c8cs00441b.
[21] K. Lu, D. Erb, M. Liu, Thermal stability and electrical conductivity of carbon-enriched silicon oxycarbide, J. Mater. Chem. C. 4 (2016) 1829–1837. doi:10.1039/c6tc00069j.
[22] J. Cordelair, P. Greil, Electrical conductivity measurements as a microprobe for structure transitions in polysiloxane derived Si-O-C ceramics, J. Eur. Ceram. Soc. 20 (2000) 1947–1957. doi:10.1016/S0955-2219(00)00068-6.

[23] P.V.W. Sasikumar, G. Blugan, N. Casati, E. Kakkava, G. Panusa, D. Psaltis, J. Kuebler, Polymer derived silicon oxycarbide ceramic monoliths: Microstructure development and associated materials properties, Ceram. Int. 44 (2018) 20961–20967. doi:10.1016/j.ceramint.2018.08.102.
[24] J. Jang, P.V. Warriam Sasikumar, F. Navaee, L. Hagelüken, G. Blugan, J. Brugger, Electrochemical performance of polymer-derived SiOC and SiTiOC ceramic electrodes for artificial cardiac pacemaker applications, Ceram. Int. 47 (2021) 7593–7601. doi:10.1016/j.ceramint.2020.11.098.
[25] P. Vallachira Warriam Sasikumar, E. Müller, P. Clement, J. Jang, E. Kakkava, G. Panusa, D. Psaltis, K. Maniura-Weber, M. Rottmar, J. Brugger, G. Blugan, In Vitro Cytocompatibility Assessment of Ti-Modified, Silicon-oxycarbide-Based, Polymer-Derived, Ceramic-Implantable Electrodes under Pacing Conditions, ACS Appl. Mater. Interfaces. 12 (2020) 17244–17253. doi:10.1021/acsami.0c01465.
[26] A.M. Wilson, J.N. Reimers, E.W. Fuller, J.R. Dahn, Lithium insertion in pyrolyzed siloxane polymers, Solid State Ionics. 74 (1994) 249–254. doi:10.1016/0167-2738(94)90217-8.
[27] M. Graczyk-Zajac, L.M. Reinold, J. Kaspar, P.V.W. Sasikumar, G.D. Soraru, R. Riedel, New insights into understanding irreversible and reversible lithium storage within SIOC and SICN ceramics, Nanomaterials. 5 (2015) 233–245. doi:10.3390/nano5010233.
[28] N. Liao, M. Zhang, B. Zheng, W. Xue, Understanding the high rate lithium storage capabilities of SiCO-derived porous carbon, Appl. Mater. Today. 18 (2020) 100434. doi:10.1016/j.apmt.2019.07.010.
[29] J. Rohrer, D. Vrankovic, D. Cupid, R. Riedel, H.J. Seifert, K. Albe, M. Graczyk-Zajac, Si-and Sn-containing SiOCN-based nanocomposites as anode materials for lithium ion batteries: Synthesis, thermodynamic characterization and modeling, Int. J. Mater. Res. 108 (2017) 920–932. doi:10.3139/146.111517.
[30] J. Kaspar, M. Graczyk-Zajac, S. Lauterbach, H.J. Kleebe, R. Riedel, Silicon oxycarbide/nano-silicon composite anodes for Li-ion batteries: Considerable influence of nano-crystalline vs. nano-amorphous silicon embedment on the electrochemical properties, J. Power Sources. 269 (2014) 164–172. doi:10.1016/j.jpowsour.2014.06.089.
[31] W. Wei, K. Xu, N. Liao, W. Xue, Insight into Si/SiCO thin films anodes for lithium-ion batteries with high capacity and cycling stability, Appl. Mater. Today. 20 (2020). doi:10.1016/j.apmt.2020.100773.
[32] D. Erb, K. Lu, Additive and pyrolysis atmosphere effects on polysiloxane-derived porous SiOC ceramics, J. Eur. Ceram. Soc. 37 (2017) 4547–4557. doi:10.1016/j.jeurceramsoc.2017.06.036.
[33] K. Xia, Z. Wu, C. Xuan, W. Xiao, J. Wang, D. Wang, Effect of KOH etching on the structure and electrochemical performance of SiOC anodes for lithium-ion batteries, Electrochim. Acta. 245 (2017) 287–295. doi:10.1016/j.electacta.2017.05.162.
[34] C. Stabler, F. Celarie, T. Rouxel, R. Limbach, L. Wondraczek, R. Riedel, E. Ionescu, Effect of composition and high-temperature annealing on the local deformation behavior of silicon oxycarbides, J. Eur. Ceram. Soc. 39 (2019) 2287–2296. doi:10.1016/j.jeurceramsoc.2019.02.024.
[35] C. Stabler, A. Reitz, P. Stein, B. Albert, R. Riedel, E. Ionescu, Thermal properties of SiOC glasses and glass ceramics at elevated temperatures, Materials 11 (2018) 1–18. doi:10.3390/ma11020279.
[36] V.S. Pradeep, M. Graczyk-Zajac, M. Wilamowska, R. Riedel, G.D. Soraru, Influence of pyrolysis atmosphere on the lithium storage properties of carbon-rich polymer

derived SiOC ceramic anodes, Solid State Ionics. 262 (2014) 22–24. doi:10.1016/j.ssi.2013.08.043.
[37] M. Wilamowska, V.S. Pradeep, M. Graczyk-Zajac, R. Riedel, G.D. Sorarù, Tailoring of SiOC composition as a way to better performing anodes for Li-ion batteries, Solid State Ionics. 260 (2014) 94–100. doi:10.1016/j.ssi.2014.03.021.
[38] M. Wilamowska-Zawlocka, P. Puczkarski, Z. Grabowska, J. Kaspar, M. Graczyk-Zajac, R. Riedel, G.D. Sorarù, Silicon oxycarbide ceramics as anodes for lithium ion batteries: influence of carbon content on lithium storage capacity, RSC Adv. 6 (2016) 104597–104607. doi:10.1039/C6RA24539K.
[39] J. Kaspar, M. Graczyk-Zajac, R. Riedel, Carbon-rich SiOC anodes for lithium-ion batteries: Part II. Role of thermal cross-linking, Solid State Ionics. 225 (2012) 527–531. doi:10.1016/j.ssi.2012.01.026.
[40] A. Tolosa, M. Widmaier, B. Krüner, J.M. Griffin, V. Presser, Continuous silicon oxycarbide fiber mats with tin nanoparticles as a high capacity anode for lithium-ion batteries, Sustain. Energy Fuels. 2 (2018) 215–228. doi:10.1039/c7se00431a.
[41] S. Martínez-Crespiera, E. Ionescu, H.J. Kleebe, R. Riedel, Pressureless synthesis of fully dense and crack-free SiOC bulk ceramics via photo-crosslinking and pyrolysis of a polysiloxane, J. Eur. Ceram. Soc. 31 (2011) 913–919. doi:10.1016/j.jeurceramsoc.2010.11.019.
[42] J. Kaspar, M. Graczyk-Zajac, R. Riedel, Lithium insertion into carbon-rich SiOC ceramics: Influence of pyrolysis temperature on electrochemical properties, J. Power Sources. 244 (2013) 450–455. doi:10.1016/j.jpowsour.2012.11.086.
[43] J. Kaspar, M. Graczyk-Zajac, S. Choudhury, R. Riedel, Impact of the electrical conductivity on the lithium capacity of polymer-derived silicon oxycarbide (SiOC) ceramics, Electrochim. Acta. 216 (2016) 196–202. doi:10.1016/j.electacta.2016.08.121.
[44] J. Kaspar, M. Graczyk-Zajac, R. Riedel, Determination of the chemical diffusion coefficient of Li-ions in carbon-rich silicon oxycarbide anodes by electro-analytical methods, Electrochim. Acta. 115 (2014) 665–670. doi:10.1016/j.electacta.2013.10.184.
[45] J. Li, K. Lu, T. Lin, F. Shen, Preparation of Micro-/Mesoporous SiOC Bulk Ceramics, J. Am. Ceram. Soc. 98 (2015) 1753–1761. doi:10.1111/jace.13541.
[46] G. Liu, J. Kaspar, L.M. Reinold, M. Graczyk-Zajac, R. Riedel, Electrochemical performance of DVB-modified SiOC and SiCN polymer-derived negative electrodes for lithium-ion batteries, Electrochim. Acta. 106 (2013) 101–108. doi:10.1016/j.electacta.2013.05.064.
[47] N. Yang, K. Lu, Porous and ultrahigh surface area SiOC ceramics based on perhydropolysilazane and polysiloxane, Microporous Mesoporous Mater. 306 (2020) 110477. doi:10.1016/j.micromeso.2020.110477.
[48] S. Martínez-Crespiera, E. Ionescu, M. Schlosser, K. Flittner, G. Mistura, R. Riedel, H.F. Schlaak, Fabrication of silicon oxycarbide-based microcomponents via photolithographic and soft lithography approaches, Sensors Actuators, A Phys. 169 (2011) 242–249. doi:10.1016/j.sna.2011.04.041.
[49] X. Xu, P. Li, C. Ge, W. Han, D. Zhao, X. Zhang, 3D Printing of Complex-type SiOC Ceramics Derived From Liquid Photosensitive Resin, ChemistrySelect. 4 (2019) 6862–6869. doi:10.1002/slct.201900993.
[50] W.L. (Simon) Law, Photochemical Metal Organic Deposition, Doctoral dissertation, Simon Fraser University (Canada), 2004.
[51] Y. de Hazan, D. Penner, SiC and SiOC ceramic articles produced by stereolithography of acrylate modified polycarbosilane systems, J. Eur. Ceram. Soc. 37 (2017) 5205–5212. doi:10.1016/j.jeurceramsoc.2017.03.021.

[52] A. Sadezky, H. Muckenhuber, H. Grothe, R. Niessner, U. Pöschl, Raman microspectroscopy of soot and related carbonaceous materials: Spectral analysis and structural information, Carbon 43 (2005) 1731–1742. doi:10.1016/j.carbon.2005.02.018.
[53] V.S. Pradeep, M. Graczyk-Zajac, R. Riedel, G.D. Soraru, New insights in to the lithium storage mechanism in polymer derived SiOC anode materials, Electrochim. Acta. 119 (2014) 78–85. doi:10.1016/j.electacta.2013.12.037.
[54] D. Erb, K. Lu, Effect of additive structure and size on SiO2 formation in polymer-derived SiOC ceramics, J. Am. Ceram. Soc. 101 (2018) 5378–5388. doi:10.1111/jace.15876.
[55] M. Patel, A.R. Skinner, A. Chaudhry, N.C. Billingham, B. Mahieu, Impact of thermal ageing on the tin catalyst species in room temperature vulcanised polysiloxane rubbers, Polym. Degrad. Stab. 83 (2004) 157–161. doi:10.1016/S0141-3910(03)00248-9.
[56] R. Zhang, Z. Zhang, K. Amine, R. West, Modification of polymethylhydrosiloxane by dehydrocoupling reactions catalyzed by transition metal complexes: Evidence for the preservation of linear siloxane structures, Silicon Chem. 2 (2005) 271–277. doi:10.1007/s11201-005-4059-6.
[57] J. Wang, V. Schölch, O. Görke, G. Schuck, X. Wang, G. Shao, S. Schorr, M.F. Bekheet, A. Gurlo, Metal-containing ceramic nanocomposites synthesized from metal acetates and polysilazane, Open Ceram. 1 (2020) 100001. doi:10.1016/j.oceram.2020.100001.
[58] J. Malinowski, D. Zych, D. Jacewicz, B. Gawdzik, J. Drzeżdżon, Application of coordination compounds with transition metal ions in the chemical industry—a review, Int. J. Mol. Sci. 21 (2020) 1–26. doi:10.3390/ijms21155443.
[59] D. Bahloul-Hourlier, J. Latournerie, P. Dempsey, Reaction pathways during the thermal conversion of polysiloxane precursors into oxycarbide ceramics, J. Eur. Ceram. Soc. 25 (2005) 979–985. doi:10.1016/j.jeurceramsoc.2004.05.012.
[60] D. Hourlier, S. Venkatachalam, M.R. Ammar, Y. Blum, Pyrolytic conversion of organopolysiloxanes, J. Anal. Appl. Pyrolysis. 123 (2017) 296–306. doi:10.1016/j.jaap.2016.11.016.
[61] N. Grassie, Recent work on the thermal degradation of acrylate and methacrylate homopolymers and copolymers, Pure Appl. Chem. 30 (1972) 119–134.
[62] G. Caminoa, S.M. Lomakin, M. Lazzari, Polydimethylsiloxane thermal degradation. Part 1. Kinetic aspects., Polymer 42 (2001) 2395–2402.
[63] H. Graetsch, A. Mosset, H. Gies, XRD and 29Si MAS-NMR study on some non-crystalline silica minerals, J. Non. Cryst. Solids. 119 (1990) 173–180. doi:10.1016/0022-3093(90)90840-I.
[64] G.D. Sorarù, S. Modena, E. Guadagnino, P. Colombo, J. Egan, C. Pantano, Chemical Durability of Silicon Oxycarbide Glasses, J. Am. Ceram. Soc. 85 (2002) 1529–1536. doi:10.1111/j.1151-2916.2002.tb00308.x.
[65] H. Bréquel, J. Parmentier, S. Walter, R. Badheka, G. Trimmel, S. Masse, J. Latournerie, P. Dempsey, C. Turquat, A. Desmartin-Chomel, L. Le Neindre-Prum, U.A. Jayasooriya, D. Hourlier, H.J. Kleebe, G.D. Sorarù, S. Enzo, F. Babonneau, Systematic structural characterization of the high-temperature behavior of nearly stoichiometric silicon oxycarbide glasses, Chem. Mater. 16 (2004) 2585–2598. doi:10.1021/cm049847a.
[66] H. Fukui, H. Ohsuka, T. Hino, K. Kanamura, Polysilane/acenaphthylene blends toward Si-O-C composite anodes for rechargeable lithium-ion batteries, J. Electrochem. Soc. 158 (2011) 550–555. doi:10.1149/1.3567956.
[67] D. Bresser, F. Mueller, D. Buchholz, E. Paillard, S. Passerini, Embedding tin

nanoparticles in micron-sized disordered carbon for lithium- and sodium-ion anodes, Electrochim. Acta. 128 (2014) 163–171. doi:10.1016/j.electacta.2013.09.007.
[68] N.G. Hörmann, A. Gross, J. Rohrer, P. Kaghazchi, Stabilization of the γ -Sn phase in tin nanoparticles and nanowires, Appl. Phys. Lett. 107 (2015) 1–4. doi:10.1063/1.4931353.
[69] G. Wang, B. Wang, X. Wang, J. Park, S. Dou, H. Ahn, K. Kim, Sn/graphene nanocomposite with 3D architecture for enhanced reversible lithium storage in lithium ion batteries, J. Mater. Chem. 19 (2009) 8378–8384. doi:10.1039/b914650d.
[70] G.B. Hoflund, G.R. Corallo, Electron-energy-loss study of the oxidation of polycrystalline tin, Phys. Rev. B. 46 (1992) 7110–7120. doi:10.1103/PhysRevB.46.7110.
[71] R.A. Powell, Auger and electron energy loss spectroscopy of oxygen chemisorption on tin, Appl. Surf. Sci. 2 (1979) 397–415. doi:10.1016/0378-5963(79)90072-2.
[72] M. Graczyk-Zajac, L. Toma, C. Fasel, R. Riedel, Carbon-rich SiOC anodes for lithium-ion batteries : Part I . Influence of material UV-pre-treatment on high power properties, Solid State Ionics. 225 (2012) 522–526. doi:10.1016/j.ssi.2011.12.007.
[73] M. Winter, J.O. Besenhard, Electrochemical lithiation of tin and tin-based intermetallics and composites, Electrochim. Acta. 45 (1999) 31–50. doi:10.1016/S0013-4686(99)00191-7.
[74] P. Kroll, Tracing Reversible and Irreversible Li Insertion in SiCO Ceramics with Modeling and Ab-Initio Simulations, MRS Proc. 1313 (2011). doi:10.1557/opl.2011.707.
[75] S. Liang, Y.J. Cheng, J. Zhu, Y. Xia, P. Müller-Buschbaum, A Chronicle Review of Nonsilicon (Sn, Sb, Ge)-Based Lithium/Sodium-Ion Battery Alloying Anodes, Small Methods. 4 (2020). doi:10.1002/smtd.202000218.
[76] K. Kravchyk, L. Protesescu, M.I. Bodnarchuk, F. Krumeich, M. Yarema, M. Walter, C. Guntlin, M. V. Kovalenko, Monodisperse and inorganically capped Sn and Sn/SnO2 nanocrystals for high-performance Li-ion battery anodes, J. Am. Chem. Soc. 135 (2013) 4199–4202. doi:10.1021/ja312604r.